v. 4, n. 16, 2024

International Journal of Human Sciences Research

"ACTIVATION OF A C_{60} FULLERENE MOLECULE BY INSERTING A FCC PT_4 PLATINUM SURFACE"

Karen De la Mora-Zarco
University of Valladolid, Department of Theoretical Physics, Atomic and Optical, Paseo de Belén, Valladolid, Spain
Division of PostGraduate Studies and Research, Technological Institute of Toluca, Metepec, Mex., Mexico

Minerva E Maya-Yescas
University of Valladolid, Department of Theoretical Physics, Atomic and Optical, Paseo de Belén, Valladolid, Spain
Division of PostGraduate Studies and Research, Technological Institute of Toluca, Metepec, Mex., Mexico

Cynthia Sinai Novoa-Ramírez
University of Valladolid, Department of Theoretical Physics, Atomic and Optical, Paseo de Belén, Valladolid, Spain
Division of PostGraduate Studies and Research, Technological Institute of Toluca, Metepec, Mex., Mexico

Abstract: The present study focused on the activation of C_{60} fullerene molecule by attacking it with an FCC Pt_4 platinum surface around the outer surface. The calculations are carried out on DFT-Quantum Molecular Dynamics level of theory as implemented in Biovia Materials Studio modeling and simulation software. DMol^3 is used to calculate total energies, electronic charge density, HOMO-LUMO energies for the treatment of global reactivity under Koopmans scheme, where energies are obtained by single point calculations. In addition, we calculate global electronic parameters that explain the reactive behavior of $C_{60}Pt_4$ complex. Based on these results: *i*) The binding energy 80.872 eV of the Pt_4C_{60}(AC) indicates that this system strongly chemisorbed. *ii*) Global electronic parameters shown indicate reactivity of activated complex. *iii*) The C_{60} (AC) exhibit an increase area of 37.39% respect to pure C_{60} molecule. *iv*) Through RDF is pore radius of 21.98 Å obtained for C_{60} (AC), which corresponds to mesoporous material for diffusion of chemical species is excellent candidate for catalytic support with applications to fuel cells.
Keywords: Fullerene (C_{60}); DFT-Quantum Molecular Dynamics; catalytic support, Platinum; Fuel cells.

INTRODUCTION

The aim of this work is to activate a fullerene molecule C_{60} by inserting a Pt_4 platinum cluster using quantum molecular dynamics (QMD). Carbon-based materials have attracted much attention due to electrocatalyst support is one of the most critical components in proton exchange membrane fuel cells (PEMFC), and generally employed to load and disperse catalytic metal nanoparticles [1–4]. The structure and proper disposal of these metal particles make low loading catalyst feasible on fuel cell operation [5,6]. The performance of PEMFCs is dominated by the activity and durability of platinum group metal (PGM) catalysts[7–10]. The supported catalyst may be greatly influenced by the interactions between metal and support, occurring at the interface between them. The so-called strong metal- support interactions (SMSIs) not only influence activity of supported metal through an improved electron transfer but also enhance stability by hindering catalyst particle migration [11]. The platinum (supported by high-surface area carbons, i.e. Pt/C) is employed as the main electrocatalyst material in both anode and cathode [12], and for a good reason. Platinum is the best single element catalyst in acidic media for the hydrogen oxidation reaction (HOR) and the oxygen reduction reaction (ORR) taking place on the two electrodes, respectively [13, 14]. The HOR (anodic process) dominates at the anode, and the ORR (cathodic process) dominates at the cathode. Besides catalytic activity, the widespread application of platinum in electrocatalysis is due to relatively good stability [15–17].

The electrocatalysts of PEM fuel cells suffer degradation, mechanism which includes dissolution, agglomeration, and/or detachment of catalytic nanoparticles [17]. Particularly, the severe corrosion of supports will accelerate electrocatalyst degradation [4,18–22]. Catalyst degradation degree is highly dependent on the interaction between catalyst nanoparticles and support materials, as well as of surface chemistry on catalyst supports [9,23]. To avoid these issues, the support materials should be chemically and electrochemically stable, having strong interaction with catalytic nanoparticles that favor electrode reactions, and stable porous structure [24–28]. In addition to great superficial area, which might be obtained through great porosity, support must also have enough electrical conductivity, so that the support act as path for flow of electrons. Furthermore, it should have a high

percentage of mesopore region (20–500 Å), to provide great accessible superficial area to both catalyst and diffusion of chemical species, these properties make good catalytic support [29,30]. The most usual materials to support catalyst nanoparticles at low-temperature PEMFCs, with high surface area are carbon blacks, e.g., Vulcan or Ketjen black [31], steam etched carbon blacks [32], and nanographite [33], which provide a higher carbon corrosion resistance associated with a higher degree of graphitic structure. However, the poor corrosion resistance which presents carbon black, currently some novel carbons and graphitized materials have been investigated which include carbon nanotube (CNT, 1D) [34–36], graphene (2D) [34–36], 3D structural carbon materials like porous carbon [37–39], carbon nanocomposites [40,41], 3D graphene [42], highly ordered porous carbon [43], graphitic carbon nitride[44], graphitic mesoporous carbon[45], and activated carbon composite support[46,47] which show greatly overcome the carbon corrosion, and exhibit improved stability.

On the other hand, activated carbon is prepared from a variety of carbonaceous precursors, and then "activated." Their preparation involves two main steps: carbonization of carbonaceous raw material at temperatures of 800°C in an inert atmosphere, and activation of the carbonized product. Thereby, all carbonaceous materials can be converted into activated carbon, although the properties of the final product will be different, depending on the nature of the raw material used, the nature of the activating agent, and the conditions of the carbonization and activation processes [48]. Generally, as the amount of activating agent increases, the porosity development (surface, and pore area) is greater, but this is accompanied by a broad pore size distribution (PSD), which explains its enormous adsorption capacity [49], and it is widely used in gas and water purification, metal extraction, in medications [50], as well as adsorbents, for gas separation, and also as catalytic supports [51,52].

Amorphous activated carbon is manufactured in many different forms: granular, fiber, and powder, as a few numbers of them [50]. The precise atomic structure of activated carbon is unknown [53]. Many theoretical studies suggest that activated carbon is derived from a type of non-graphitic carbon (it cannot be converted to graphite even whether heated to 3000 °C). This non-graphitic carbon is composed of disordered graphite sheets and consists of sp^2 carbon atoms [53, 54]. Similarly, activated carbon surface through transmission electron microscopy (TEM) shows that non-graphitic carbon is composed of pentagonal and hexagonal rings [55, 56]. The C_{60} fullerene possesses a stable structure, and it has icosahedral geometry I_h, and 180° of freedom for each C_{60} molecule. The symmetry of icosahedron for C_{60} fullerene might be increased by applying a number of balance methods [57–59]. This molecule has only 46 frequency degrees of freedom that this forms are expected in routine way [60]. It is based on a population of icosahedron structure of C_{60} that is corresponded with the symmetry form. Therefore, all the carbon atoms of fullerene, which show sp^2 hybridization, are equivalent. The sp^2 atoms of C_{60} cause certain little pyramidal form, given that all double bonds deviate from planarity due to the spherical shape of the molecule, which gives it certain tension responsible for its reactivity. In most reactions, a decrease in tension occurs while the sp^2 hybridization carbons pass to sp^3. The C_{60} has good acceptor capacity similar to other organic molecules such as benzo and naphthoquinones. Theoretical calculations predict low energy triple degenerate LUMO for the C_{60} molecule, so you would expect it to accept a maximum of 6 e^- [61].

In recent years, some of the C_{60} fullerene applications doping chemically using heteroatoms (e.g., N, S, O, Si, and P), have been the focus of intensive researches owing to their unique geometries, physical properties and potential applications in nanotechnology [62]. Due to its curvature and pentagon defect compared with graphene and carbon nanotube, which might make fullerene a better choice for ORR [63]. Also, fullerene decorated with alkali metals (AM) or alkaline earth metals (AEM) improves the hydrogen storage capacity [64]. Most of the fullerene chemistry has been carried out with C_{60}, as this is the most symmetrical and abundant fullerene. In this sense, experimental evidence suggests that activated carbon has structure similar to that of fullerenes, therefore this model allows an understanding of adsorption phenomena compared to traditional model based on graphite sheets [65, 66]. Hence, the use of fullerene type structures in the simulation of activated carbon behavior is appropriate [66].

In this work, we carried out DFT-Quantum Molecular Dynamics calculations for activation of one C_{60} fullerene molecule by inserting one platinum FCC Pt_4 cluster into its outer surface, to evaluate its use as catalytic support. We found that by placing FCC Pt_4 over a hexagonal ring (a_h) of the C_{60} fullerene molecule, it is viable for the insertion of this FCC Pt_4 into the fullerene molecule. Therefore, the fullerene is activated, and an activated $C_{60}Pt_4$ complex is formed. The adsorption energy of the $C_{60}Pt_4$ complex corresponds to chemisorption with an increase of 18.93 % area of $C_{60}Pt_4$ complex with respect to the pure C_{60} and shows a bandgap value of 0.09 eV indicating it is a conductor material ideal for catalytic supports. Through RDF we calculated an approximation of pore radius for this C_{60}(AC) resulting in a value of 21.98 Å, which is in the range of mesoporous material facilitating the diffusion of chemical species, and we calculated the global electronic parameters showing values of -5.887 eV, 0.045 eV, 11.11 eV^{-1}, 5.842 eV, 5.932 eV, and 385.06 eV for chemical potential, hardness, softness, electronic affinity, ionization potential, and electrophilicity, respectively. This explains the reactive behavior of $C_{60}Pt_4$ complex making it a suitable candidate to meet requirements established for catalytic support.

CALCULATION METHOD

In this work, DFT calculations are carried out using Biovia Materials Studio $Dmol^3$ software [67, 68]. The exchange and correlation function is applied using the generalized gradient approximations (GGA), and Perdew Burke and Ernzerhof (PBE) [69] functional, which provides good results in the calculation of equilibrium geometries for fullerene type compounds [70, 71], with a set of double numerical bases (dnd). The set of bases have the advantage of being equivalent to the Gaussian base 6-31G* for spin unrestricted since some studies of fullerene type carbonaceous systems use this set of bases that adequately describe the electronic structure [72,73].

DFT molecular dynamics (QMD) was carried out in the NVE canonical ensemble at 300ºK with a step time of 1 fs and a total number of 150 steps for each dynamic using a maximum of 1000 cycles with an SCF tolerance of 1×10^{-6}. The convergence tolerance for energy change, maximum force, and maximum displacement was 2×10^{-5} Ha, 0.004 Ha/Å, and 0.005Å, respectively. All structures were optimized until the forces were less than 0.002 Ha/Å. $DMol^3$ module is used to calculate total energy, electronic charge density, HOMO- LUMO energies for the treatment of reactivity globally addressed under the Koopmans scheme, where energies are obtained by single-point calculations with the Hartree-Fock method[74]. In addition, Electrostatic Potential, Density of States

(DOS), and Partial Density of States (PDOS) are calculated.

The calculations of the area of the C_{60} fullerene molecule before QMD have been carried out by inserting triangles in each amorphous carbon ring and using Heron's formula [50]:

$$A = \sqrt{(P(P-a)(P-b)(P-c))} \quad (1)$$

where $P=(a+b+c)/2$ is the perimeter of a triangle of a, b, c sides.

The area of C_{60} molecule after performing QMD is calculated using the radial distribution function g(r) (pair correlation function[75, 76]), which is a very useful quantity in molecular dynamics. This quantity represents the average distribution of atoms around any given atom within the system. This information can be used to calculate the coordination number, crystallinity, and more, given that several macroscopic thermodynamic properties of liquids can be expressed in terms of g(r). A radial distribution function g(r) can be directly obtained by taking all distances from the center of the system to each atom of it, which in this case is from the center of C_{60} fullerene to each carbon atom of the same. This calculation is normalized by using the following equation:

$$g(r) = 4\pi r^2 \rho dr \quad (2)$$

where r is distance, ρ is numerical density of the system, and dr is volume. In this case the numerical density is:

$$\rho = \frac{N_{particles}}{Volume} \quad (3)$$

The number N of particles is 60 carbon atoms of fullerene, and the volume is calculated using the software Atoms and Volume of Materials Studio. The area under the curve of (RDF) was calculated with the mathematical software of dynamic geometry GeoGebra programmed in java, it allows the dynamic drawing of geometric constructions of all kinds as well as the graphic representation, the algebraic treatment, and the calculation of real functions of variable real, its derivatives, integrals, etc.

The binding energies of the compounds are determined on the basis of equation [77]:

$$E_{ad(C_{60}Pt_4)} = E_{C_{60}Pt_4} - E_{C_{60}} - E_{Pt_4} \quad (4)$$

where E_C60Pt4 is the total energy obtained from the geometry optimization calculation of the C_{60} + Pt_4 system, E_C60 is the energy of isolated fullerene molecule C_{60}, and $E_{Pt}4$ is the energy of the isolated Pt_4 cluster.

Global electronic indexes, as defined within the density functional theory of Parr, Pearson and Yang [78–80] are useful tools to understand the reactivity of molecules in their ground states. For instance, the electronic chemical potential μ describing the changes in electronic energy with respect to the number of electrons is usually associated with the charge transfer ability of the system in its ground state geometry. It has been given a very simple operational formula in terms of the one electron energies of the frontier molecular orbitals HOMO and LUMO, E_{LUM0} and E_{H0M0}, as[78, 81]

$$\mu \approx \frac{1}{2}(E_{LUM0} + E_{H0M0}) \quad (5)$$

with the requirement of an entire population of molecular orbitals, it leads to ionization potential (I) and electronic affinity (A) [79, 82]

$$A = -E_{LUM0} \quad (6)$$

$$I = -E_{H0M0} \quad (7)$$

Parr and Pearson, identify chemical hardness as the second derivative of energy with respect to the number of electrons at a fixed external potential [83, 84], and can be understood as the resistance 5 to change of the electronic distribution of the system. It is determined numerically by approximations

based on finite differences, indicating that the hardness is related to the "gap" of energy between occupied and unoccupied orbitals. The softness (S) is the inverse chemical hardness (5) and constitutes a useful concept on the prediction of chemical reactivity, as shown in the following expressions [82, 85]:

$$5 \approx \frac{1}{2}\left(E_{LUM0} - E_{H0M0}\right) \tag{8}$$

$$S = \frac{1}{25} \tag{9}$$

In terms of the electronic chemical potential μ and the chemical hardness 5, defined in Eq. (2) and Eq. (5), the electrophilicity index encompasses both, the propensity of the electrophile to acquire an additional electronic charge driven by μ^2, and the resistance of the system to exchange electronic charge with the environment described by 5, simultaneously. A high value of μ and a low value of 5 therefore characterize a good electrophile. The electrophilicity power has been given as the following simple expression [81,86–88]:

$$\omega = \frac{\mu^2}{25} \tag{10}$$

RESULTS AND DISCUSSION

The fullerene molecule C_{60} consists of 60 carbon atoms in a spherical structure of radius 3.557 Å composed of hexagonal and heptagonal rings. Its structure contains 20 hexagonal and 12 pentagonal faces, a surface area of 1105.33Å^2, symmetry I_h [89], and bond lengths of 1.451 Å and 1.399 Å, for single and double bonds respectively, according to literature [90– 92], as shown in Figure 1. The platinum cluster Pt_4 was constructed according to literature [93, 94], its surface area is 103.30 Å^2, type symmetry T_d, and bond length of 2.71Å [95, 96], as shown in Figure 2.

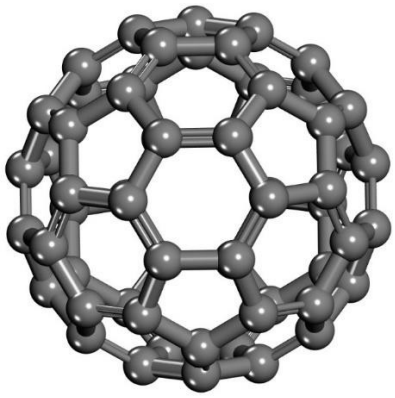

Figure 1. Geometry optimization of C_{60} fullerene molecule.

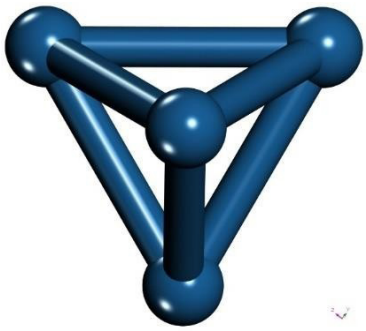

Figure 2. Geometry optimization of Pt_4 platinum cluster.

The highest occupied molecular orbital (HOMO) and the lowest unoccupied molecular orbital (LUMO) are used to determine the charge transfer and molecular interactions with other species. The energy difference between HOMO and LUMO, called bandgap energy, plays an important role in determining the chemical stability and reactivity of the molecule [97, 98]. The HOMO and LUMO molecular orbitals are shown in Figures 3 and 4, for the case of the C_{60} molecule and Pt_4 cluster, respectively. The blue lobes show positive values, and negative values correspond to the yellow lobes of the wave function. Because of the high symmetry properties of C_{60}, the HOMO and LUMO distributions are almost on the whole fullerene cages, these are six-fold and four-fold degeneracies respectively, for LUMO degeneracies essentially represent

the fullerene property as strongly electron acceptors (Figure 3a), and the distribution of the electronic density HOMO in this region there is a pair of electrons that the molecule might easily yield (Figure 3a) [99]. For the Pt_4 cluster, the distribution of HOMO and LUMO are located mainly in the Pt atoms, which implies that these positions are the active centers. The distribution of the electronic density HOMO lies on the platinum atoms since in this region there are a pair of electrons that the cluster can easily lose (Figure 4a). The distribution of LUMO (the place of the lowest orbitals that are empty) is also found on the platinum atoms, (Figure 4b) [100].

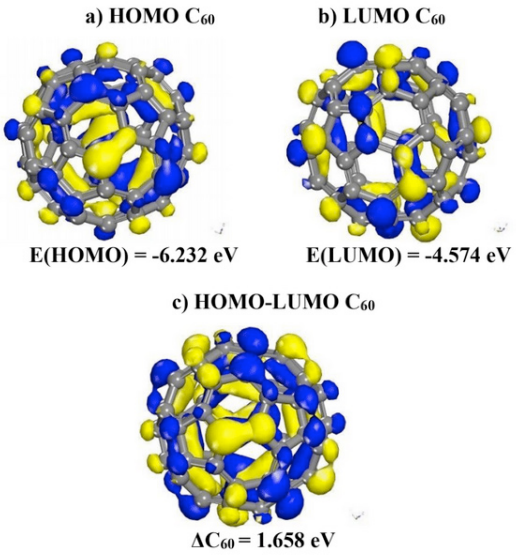

Figure 3. Analysis of the spatial HOMO-LUMO distribution of the C60 molecule, the blue lobes show positive values and the yellow lobes negative values of the wave function a) HOMO analysis, b) LUMO analysis, c) HOMO – LUMO analysis of the C60 molecule with an energy difference ΔC60 = 1.658 eV

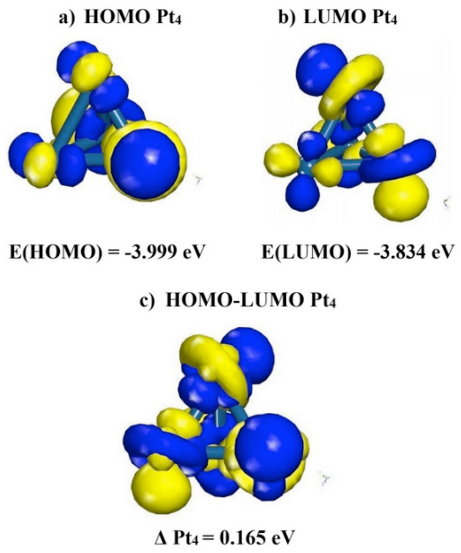

Figure 4. Analysis of the spatial distribution HOMO-LUMO of the Pt_4 molecule. The blue lobes show positive values and the yellow lobes negative values of the wave function a) HOMO analysis, b) LUMO analysis, c) HOMO – LUMO analysis of the Pt_4 cluster with an energy difference $\Delta Pt_4 = 0.165eV$.

The electronic properties in organic and inorganic systems depend on the HOMO and LUMO border orbitals. The molecular orbitals extend between all the atoms in a molecule and are linear combinations of atomic orbitals, the molecular orbitals that interact are generally the highest occupied molecular orbital HOMO and the lowest unoccupied molecular orbital LUMO. The calculations of the HOMO-LUMO energy difference or gap (Δ) for the fullerene molecule C_{60} and the platinum cluster Pt_4 are summarized in Table 1. It is observed that the energy difference value for the fullerene molecule C_{60} is 1.658 eV. For the FCC Pt_4 cluster, the energy difference is 0.165 eV. This indicates that platinum FCC cluster tends to easily share electrons.

System	HOMO (eV)	LUMO (eV)	(Δ)
Pt_4	-3.999	-3.834	0.165
C_{60}	-6.232	-4.574	1.658

Table 1. HOMO-LUMO energy difference or gap (Δ) of C_{60} molecule and the Pt_4 cluster.

The energies of the bands are plotted with respect to the Fermi level, to which a value of zero is assigned. It is observed in Figures 5 and 6 for the C_{60} molecule and Pt_4 platinum cluster, that the band interval at point Q is 1.67 eV and 0.171 eV, respectively. This indicates that the C_{60} molecule is a semiconductor material similar to GaAs [92], while for FCC Pt_4 cluster the band gap value is similar to that one of Pt_9 platinum cluster [94].

To analyze the electronic structure of the C_{60} molecule and the Pt_4 cluster, the DOS and PDOS calculations have been carried out. We focus on *p* orbitals of carbon atoms in C_{60} molecule, and *d* orbitals of platinum atoms [95] in Pt_4 cluster, for each independent system. Figure 7 shows density of states (DOS) and Figure 8 shows partial density of states (PDOS) for C_{60} molecule. The *p* orbitals of C_{60} molecule play the main role in accepting electrons (Fig. 7) due to their relatively high ionization potentials, which leads to the orbital locations (Fig. 8).

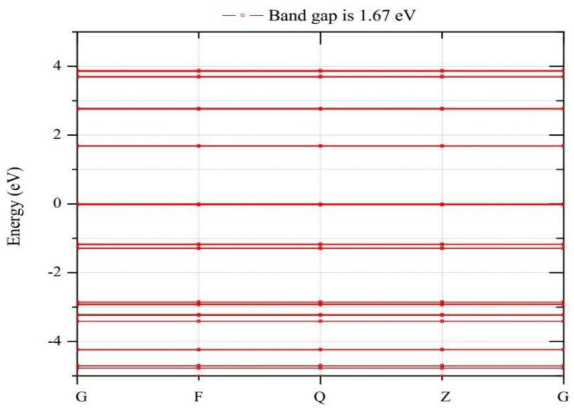

Figure 5. Band gap of the C_{60} fullerene molecule.

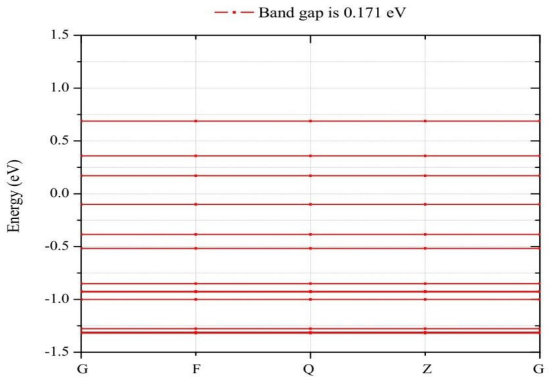

Figure 6. Band gap of Pt_4 cluster.

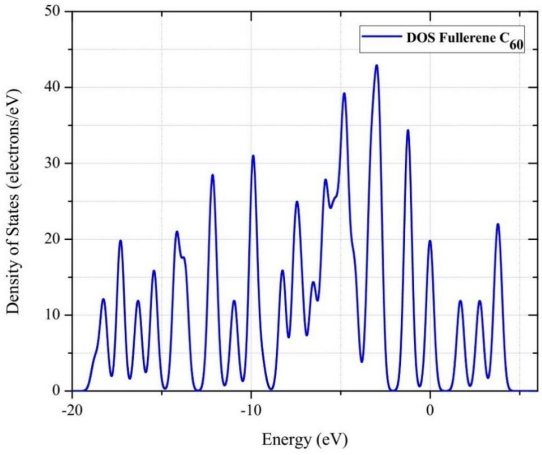

Figure 7. The *p* orbitals of C_{60} molecule by means of Density of States (DOS).

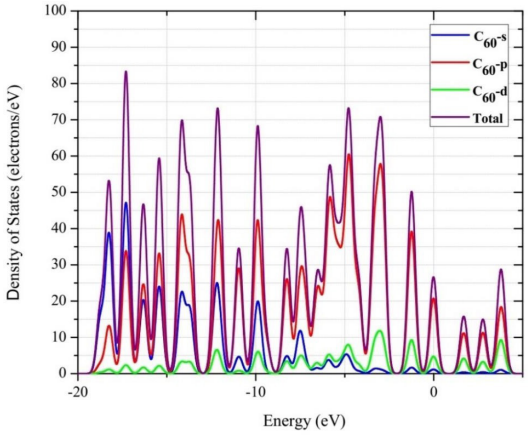

Figure 8. Partial Density of States (PDOS) of C_{60} molecule showing *s*, *p* and *d* orbitals.

Figure 9 shows DOS and Figure 10 shows PDOS of Pt_4 cluster. The *d* orbitals at Pt_4 cluster represent the main role to donate electrons (Figure 9), due to their relatively low ionization energies, which leads to delocalization of the orbitals (Figure 10).

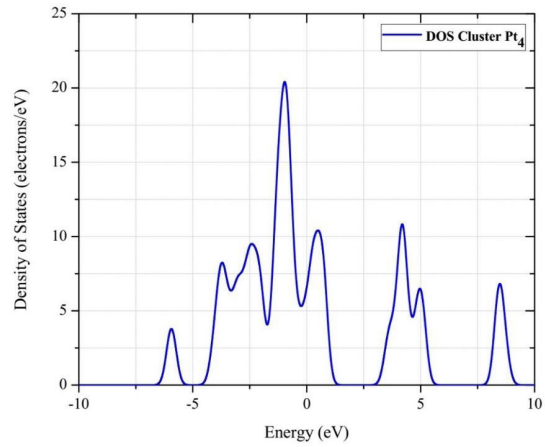

Figure 9. The *d* orbitals at Pt_4 cluster by means of Density of States (DOS).

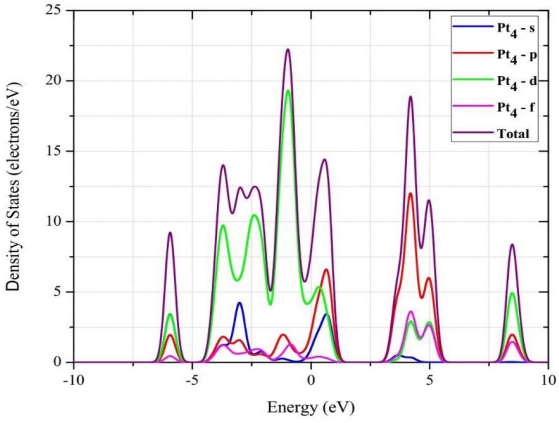

Figure 10. Partial Density of States (PDOS) of the Pt_4 cluster showing *s*, *p*, *d* and *f* orbitals.

Table 2 shows the reactivity parameters of the two structures: FCC Pt_4 cluster and C_{60} molecule. The parameters explain the reactive behavior of these two systems as shown in Figure 11, where chemical potential, hardness, affinity, and ionization potential of both C_{60} and Pt_4 are similar, and the electrophilicity of C_{60} is approximately 5 times lower than that of Pt_4. The chemical potential μ calculated in these two systems shows the tendency of electrons to escape from an equilibrium system, so that, a good electron donor (as $\mu_{Pt}4$) outcomes when electrons flow from higher to lower regions of chemical potential (as μ_C60), which is a good electron acceptor. Then, with these high and low potentials, there is a possibility that a molecule produces or accepts electrons, which favors electronic transfer [85,101].

There is a relationship between chemical hardness η and system stability, so that, the molecular system becomes more stable when chemical hardness increases, the calculated value of chemical hardness of fullerene molecule C_{60} (5_C60) is found to be higher than that one obtained from the platinum cluster Pt_4 ($5_{Pt}4$), which indicates greater difficulty of electrons to leave C_{60} molecule than for the Pt_4 cluster [85]. The calculated electronic affinity values of C_{60} molecule (A_C60) show a characteristic great value in systems that can easily accommodate an excess of electrons coming from the surroundings compared to the Pt_4 (A_{Pt}) platinum cluster [101]. The ionization potential values of the C_{60} molecule (I_C) are the greatest, this indicates the tendency of fullerene molecule to bring or accept a pair of electrons, therefore in the case of Pt_4 cluster ($I_{Pt}4$), the obtained values represent the main role to donate electrons [88]. The electrophilicity index of Pt_4 cluster (ω_{Pt}) is greater than that of fullerene molecule C_{60} (ω_C60), this increase in electrophilicity is in accordance with strong electrophiles, since they exceed the value of ω> 1.5 eV [81], so it results in a great acceleration of a chemical reaction. Therefore, due to catalyst ($\omega_{Pt}4$) effect, the strong increase in electrophilicity value can be explained [81].

System	μ (eV)	A (eV)	I (eV)	y (eV)	S $(eV)^{-1}$	ω (eV)
Pt_4	-3.916	3.834	3.999	0.0825	6.06	92.90
C60	-5.403	4.574	6.232	0.829	0.6031	17.60

Table 2. Reactivity parameters of the C_{60} fullerene molecule and the Pt_4 cluster

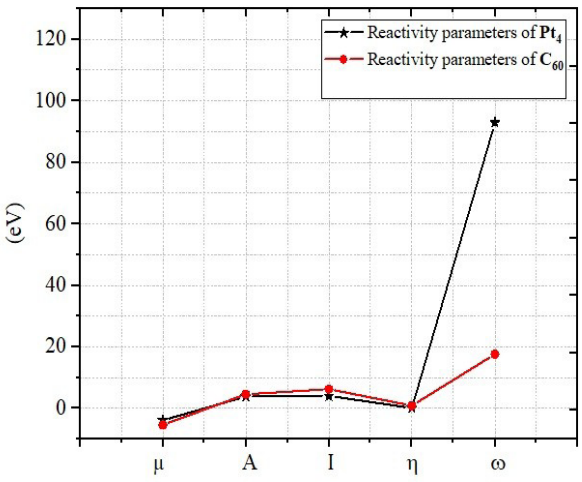

Figure 11. Global descriptors of reactivity.

Electronic density and electrostatic potential are significant characteristics in reactivity, as shown in the C_{60} molecule and Pt_4 cluster, becoming useful application to predict the reactivity of molecules on each space point. It allows visualizing space regions towards which atoms are attracted positively or negatively (regions of either positive or negative electrostatic potential) [47] The electrostatic potential maps are shown in Figure 12, allowing visualization of how electrons are distributed in the two structures: C_{60} molecule (Figure 12a), and Pt_4 cluster (Figure 12b). The red regions indicate high electronic density, while blue regions indicate low electronic population. The intermediate states follow rainbow order from the center to external border, according to the major or minor presence of electrons, and thus green and yellow colors close to the center border of the structure indicate homogeneous electronic balance.

Carbon atoms possessing the same electronegativity should give an almost homogeneous electronic distribution, and there is no preferential place where electrons are circulating, but our map tells us that the external part of the C_{60} fullerene structure and bonds of Pt_4 cluster have higher electronic density; therefore Pt_4 cluster is oriented toward the center of a hexagonal face (*ah*) of C_{60} molecule, with bonds of Pt_4 cluster over single bonds of a hexagonal ring of C_{60} molecule, and it is the input configuration feasible to carry out molecular dynamics as shown in Figure 12 (c).

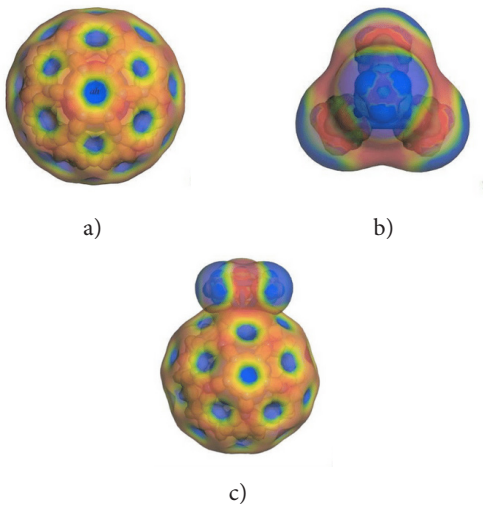

Figure 12. Electronic density and electrostatic potential. a) Fullerene, b) Pt_4 cluster, c) Orientation of Pt_4 cluster attacking fullerene.

The Pt_4 cluster enters through the center of a hexagonal face of the C_{60} fullerene, at distance of 1.7 Å from the inserted Pt into the fullerene to the nearest carbon atoms, as shown in Figures 12c and 13a; this is the input configuration system for molecular dynamics calculation. The output after 100 steps of molecular dynamics is shown in Figure 13b, where it is observed that Pt_4 cluster open the fullerene in a hexagonal carbon ring of the C_{60} molecule, the bonds are broken without liberating any carbon atom, and according to literature this corresponds to activated carbon (AC) structure [55, 66]. In this sequence, Pt_4 cluster has been now set inside to the new C_{60}(AC) molecule for a second molecular dynamics, which is carried out in 30 steps, and its output shown in Figure 13c. Then, a new C_{60}(AC) molecule is now observed as a deformed carbon nanotube. In the third molecular dynamics of 15 steps of this sequence, it is observed (Figure 13d) that Pt_4

cluster has been set closer to the exit side, with tendency to leave from the new deformed C_{60}(AC) molecule. In the fourth molecular dynamics of 50 steps, we can see how the Pt_4 cluster of the already deformed C_{60}(AC) molecule has been set emerging, as shown in Figure 13e, and the fifth molecular dynamics of 50 steps, the Pt_4 cluster is outside of the final form of the C_{60}(AC) molecule (Figure 13f) forming a Pt_4C_{60}(AC). Considering this final form of the system after whole molecular dynamics as shown in Figure 14, the average length among two carbon atoms (C-C) is 1.404Å bond, which according to Harris the experimental result exhibits 1.42 Å [55, 56] value. The difference among theoretical and experimental results is 1.13%.

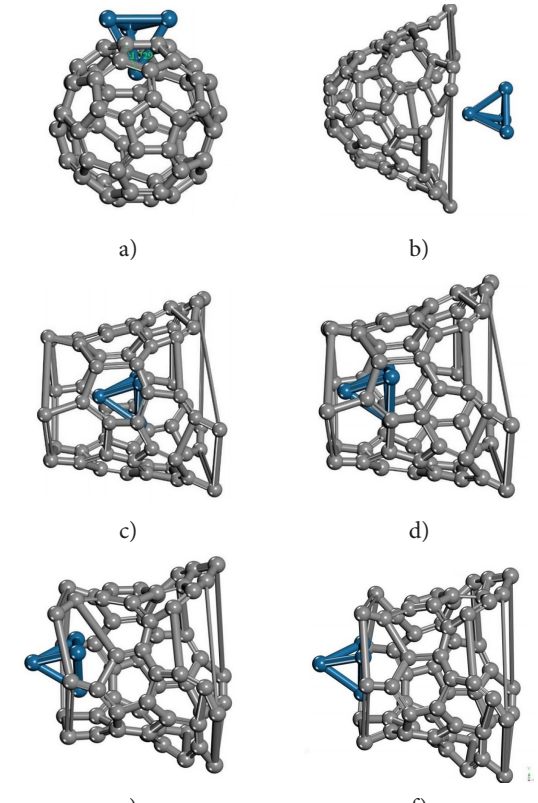

Figure 13. DFT Molecular Dynamics (QMD) to obtain Pt_4C_{60} complex outputs: a) Input Pt_4+C_{60}, b) 1st QMD output of 100 steps, c) 2nd QMD output of 30 steps, d) 3rd QMD output of 15 steps, e) 4th QMD output of 15 steps, f) 5th QMD output of 50 steps. The gray and dark blue spheres represent the C and Pt atoms, respectively.

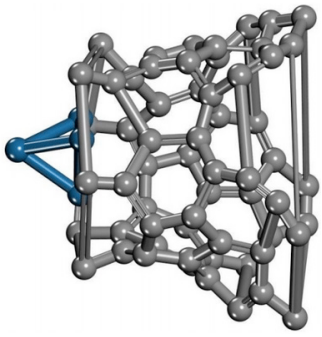

Figure 14. Pt_4C_{60}(AC) complex.

The Kekulè connectivity calculations for Pt_4C_{60}(AC) complex are shown in Figure 15a, where bond length tolerance is 0.6 to 1.15 Å. The adsorption energy of the system is calculated using equation (1). The total energy obtained from the geometry optimization of doped complex, fullerene molecule and the isolated platinum cluster is $E_{Pt}4C60 = 385.449\ eV$, $E_C60 = 455.546\ eV$, and $E_{Pt}4 = 10.775\ eV$, respectively. Therefore, the adsorption energy value of this doped complex is $E_{ad}\ of\ Pt_4C_{60} = 80.873\ eV$. Hence, there is a covalent bond between FCC Pt_4 cluster and C_{60} fullerene molecule [95, 102], indicating that the system is strongly chemisorbed according to the range handled by Atkins [103, 104]. This indicates that it is electrochemically stable since it has a strong interaction with catalytic nanoparticles, which is in agreement with what was stated by Kim *et al.*[105] and Antolini [30] for catalytic support. According to Figure 15a, the bonds of both hexagonal faces of C_{60} molecule have been broken, where the Pt_4 cluster is inserted and exited, none carbon atom in the molecule is detached, and according to literature, it is an activated complex C60Pt4 [55, 66, 104].

Pore radius of C_{60} activated (Figure 15b) has been approximated to 21.98 Å through analysis of Forcite module the Radial Distribution Function (RDF) [30, 106] (6.18 times of that for original fullerene), a diameter of 43.96Å, and a superficial area of 1518.715 $Å^2$ (see Appendix). Fullerene

C_{60} activated is mesoporous, the particles of the FCC Pt_4 catalyst remain supported on the surface, in the pores of this mesoporous carbon. This agrees with that mentioned by Antolini [30]: the catalytic support must have the property of being a mesoporous material. This mesoporous surface gives rise to a highly effective surface area accessible to the catalyst, has high catalytic activity, provides electron flow transport, and stimulates chemical diffusion of species, as a catalytic supported [11, 105, 30, 106].

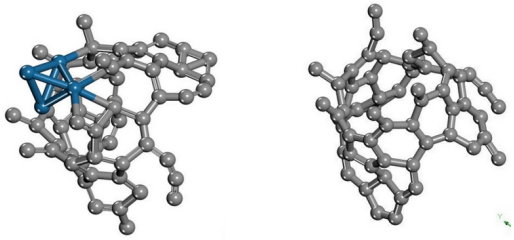

a) b)

Figure 15. (a) Kekulè connectivity of the $C_{60}Pt_4$ complex, (b) C_{60} activated

Figure 16 represents the molecular orbitals HOMO and LUMO for the case of $C_{60}Pt_4$ complex. The blue lobes show positive values (bonding) and yellow lobes for negative values (antibonding) of the wave function. For the system (Figure 16a) the distribution of the HOMO electronic density is found in the double bonds and in the platinum cluster, in this region, there is a pair of electrons that can easily be given by the system. As it can be seen, the distribution of LUMO is over carbon atoms, a place of the lowest empty orbitals (Figure 16b).

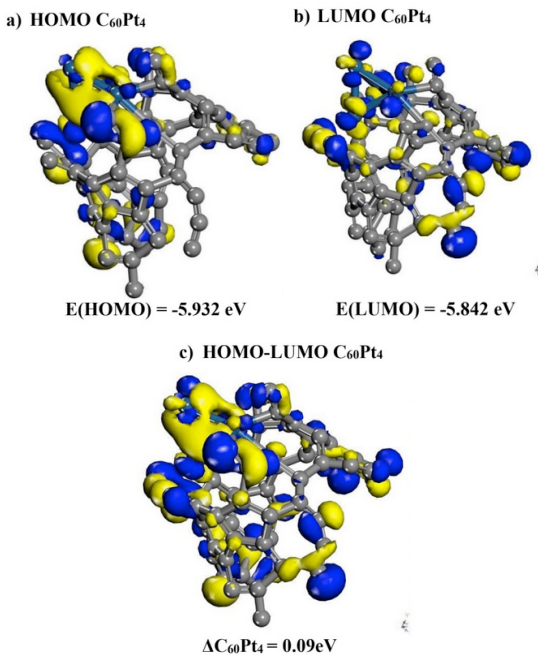

Figure 16. HOMO-LUMO spatial distribution analysis of the $C_{60}Pt_4$ complex, bonding and antibonding wave functions correspond to blue and yellow lobes, respectively, a) HOMO analysis, b) LUMO analysis, c) HOMO – LUMO analysis of $C_{60}Pt_4$ complex, with an energy difference $\Delta C_{60}Pt_4$ = 0.09eV.

The calculation of the HOMO-LUMO energy difference or gap (Δ) for the $C_{60}Pt_4$ complex is summarized in Table 3. It is observed that their energy difference is 0.09eV. This indicates that it is relatively easy for this complex to adsorb metallic particles, and it can act as a route for the flow of electrons, facilitating the transport of charge during the process. This is consistent with what was mentioned by Cherevko *et al.* [17], Antolini [30] and Modak *et al.* [90] about that catalytic support must have good electrical conductivity.

The band energies are plotted with respect to the Fermi level, which has zero value assigned. In Figure 17, it is observed that the band gap at Q point reduced to 0.09eV, behaves as conductor for $C_{60}Pt_4$ system. This fact facilitates the flow of electrons during the

System	HOMO (eV)	LUMO (eV)	(Δ)	μ (eV)	A (eV)	I (eV)	y (eV)	S $(eV)^{-1}$	ω (eV)
$C_{60}Pt_4$	-5.932	-5.842	0.09	-5.887	5.842	5.932	0.045	11.11	385.06

Table 3. HOMO-LUMO energy difference or gap (Δ) and reactivity parameters of $C_{60}Pt_4$ complex

process as catalytic support [17, 30].

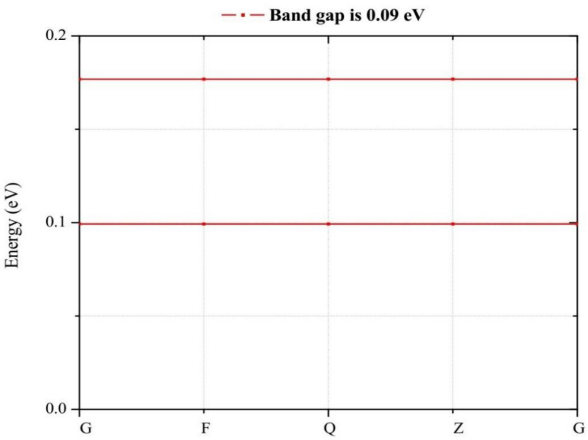

Figure 17. Band gap of $C_{60}Pt_4$ System.

The Density of States (DOS) and Partial Density of States (PDOS) analysis is an effective method to understand the interaction between Pt_4 cluster and C_{60} molecule to get $C_{60}Pt_4$ complex. In the process of bond formation, valence electrons achieve a fundamental role. We focus on *p* and *d* orbitals of carbon and platinum atoms of $C_{60}Pt_4$ complex. Figures 18, and 19, exhibit density of states (DOS), and partial density of states (PDOS), of $C_{60}Pt_4$ complex, respectively. The *p* orbitals of C_{60} molecule take the main role in accepting electrons (Figure 18) due to their relatively high ionization potentials, which leads to orbitals location (Figure 19). The *d* orbitals of Pt_4 cluster represent the main role to donate electrons, due to their relatively low ionization energies, which leads to orbitals delocalization (Figure 19).

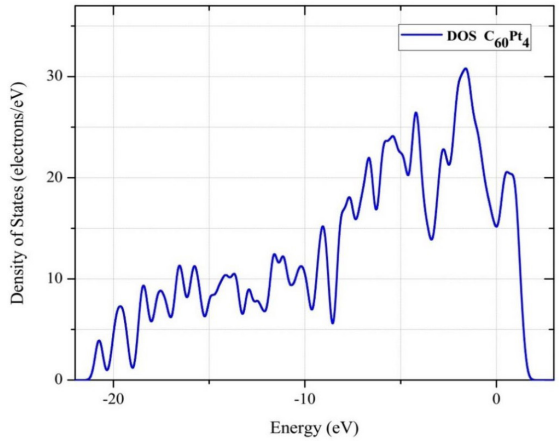

Figure 18. The *p* orbitals of the $C_{60}Pt_4$ complex using Density of State (DOS).

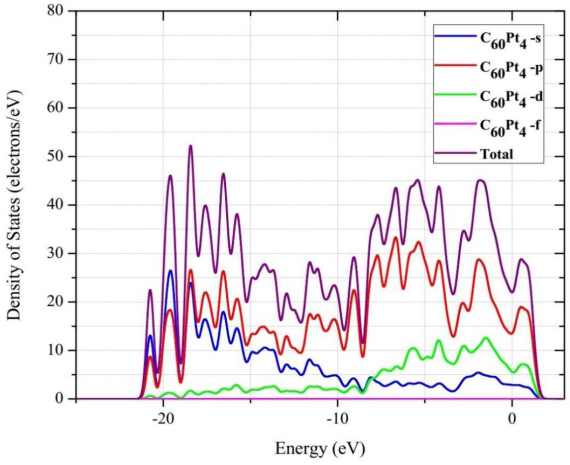

Figure 19. Partial Density of States (PDOS) of the $C_{60}Pt_4$ complex showing *s, p, d* and *f* orbital states.

When Pt_4 cluster is compatible with C_{60} fullerene, the sharp peak near to Fermi level for *p* orbital of carbon weakens, and orbital *d* of Pt_4 cluster moves towards the lowest energy. Together overlap completely, this means that platinum orbital hybridizes with *p* orbital of carbon. Therefore, there is a strong covalent interaction between the platinum and carbon atoms with greater adsorption energy, which improves the stability of the catalyst [95, 107].

Table 3 shows the reactivity parameters of the $C_{60}Pt_4$ complex. The chemical potential calculated for $C_{60}Pt_4$ system is $\mu_C 60Pt4 = -3.205$ eV, and indicates that there is a possibility that a molecule produces or accepts electrons, which favors electronic transfer, compared to the value of a non-functionalized activated carbon [54]. There is a relationship between chemical hardness η and system stability, so that the molecular system improves its stability when its chemical hardness increases. The calculated chemical hardness value ($5_C 60Pt4$) has been found to be lower compared to the structure value of a non-functionalized activated carbon, indicating less difficulty of electrons to leave from $C_{60}Pt_4$ complex [54, 85]. The electronic affinity ($AC60Pt4 = 0.535\ eV$) calculated value exhibit characteristic great value in systems that can easily accommodate an excess of electrons, coming from the surroundings compared to the values obtained from a non-functionalized activated carbon [54]. The ionization potential values of the system ($I_C 60Pt4$) are higher, this indicates the tendency of the system to bring or accept a pair of electrons, therefore, it facilitates charge transport, compared to the value of the structure of non-functionalized activated carbon $I_C 60Pt4$ =5.875eV [54]. The electrophilicity index ($\omega_C 60Pt4$) calculated is greater than the structure value of an non-functionalized activated carbon of $\omega_C 60Pt4$ = 1.924 eV [54], in addition, it is greater than ω > 1.5 eV value, and considered as strong electrophiles. Therefore, the effect of the catalyst allows the reaction rate to be improved, this is due to the strong increase in the electrophilicity power of ($\omega_{Pt} 4$) [81], in this way, electrophilicity, results in an increase in charge transfer, with an improvement in the reaction rate since it increases its catalytic activity by being supported on the C_{60} molecule.

CONCLUSIONS

We carried out the activation C_{60} fullerene molecule by inserting FCC Pt_4 cluster since its outer surface, by attacking as an inverted pyramid toward a hexagonal (*ah*) face of C_{60} fullerene, with the bonds of Pt_4 staying over single bonds of C_6 ring of fullerene. We found that it is a good orientation for insertion of cluster into fullerene for achieving the activation using Materials Studio Dmol^3 program. First, by DFT-QMD calculations, FCC Pt4 cluster is inserted into a C_{60} fullerene by breaking C-C bonds after geometry optimization. We obtained an increased area of 37.39 % for C_{60} (AC) with respect to the pure C_{60}, making the evaluation of this complex as catalytic support due to the large surface area shown during the activation, facilitating electron transfer, resulting in better device performance. We also calculate the binding energy of the $C_{60}Pt_4$ complex, showing a value of 80.872eV indicating that the system is strongly chemisorbed. Second, the $C_{60}Pt_4$ complex shows values of 5.93 eV and 5.84 eV for HOMO and LUMO respectively, with a bandgap of 0.09 eV indicating that it is a conductor material. Besides, the *d* orbitals of platinum FCC Pt_4 cluster move towards the lowest energy level, and the energy region overlaps well with that of *p* orbitals of C_{60} fullerene that improve the stability of the platinum catalyst. Third, through radial distribution function (RDF) the pore radius 21.98 Å of the molecular complex is calculated, being a mesoporous material (20–500 Å) that facilitates diffusion of chemical species as required according to literature. In addition, in a mesoporous carbon support catalyst, the metal catalyst particles are distributed and supported on the surface or in the pores of the mesoporous carbon. A mesoporous surface area gives rise to high dispersion of Pt particles, which resulted in a large effective surface area of Pt with high

catalytic activity. The mesoporous structure also facilitates smooth mass transportation to give rise to high limiting currents. Fourth, we calculated the global electronic parameters that show values of -5.887 eV, 0.045 eV, 11.11 eV-1, 5.842 eV, 5.932 eV, and 385.06 eV for chemical potential, hardness, softness, electronic affinity, ionization potential, and electrophilicity respectively, that explained the reactive behavior of $C_{60}Pt_4$ complex, resulting in an increase in charge transfer, with an improvement in the reaction rate since it increases its catalytic activity when the Pt_4 cluster is supported on the C_{60} molecule. According to these results, the C_{60} (AC) is an excellent candidate for catalytic support with applications to fuel cells.

APPENDIX

The pore size of the carbon C_{60} activated is approximated by means of radial distribution functions (RDF). First, through a cubic cell has been built in the Amorphous Cell Tools module of BIOVIA Materials Studio, with dimensions of 66.9 Å per side, a density of 0.004 g/cm^3, and a temperature of 298 K. The activated C_{60} system is introduced in this cell and using analysis of Forcite module the Radial Distribution Function, as seen in Figure A1. These dimensions have served to cover an approximate diameter of the activated C_{60} carbon molecule, and contrast with the results obtained here below, through polynomial fits for manual calculations of g(r).

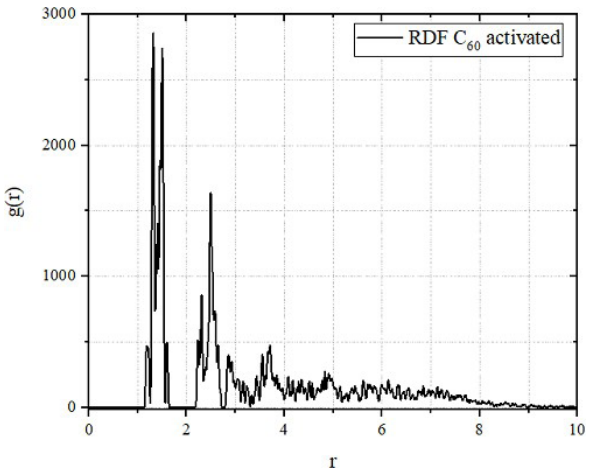

Figure A1. Area under the curve of the g(r) (or RDF) of the carbon C_{60} activated.

An approximation to pore size is obtained through the radius by using circle area $A = \pi r^2$ through the equation $r = \sqrt{A}_{\pi}$ and diameter $d=2r$.

The area under the curve of this g(r) is 1518.715 Å^2, so the pore size of this activated C_{60} carbon molecule is r = 21.98 Å, which implies a pore diameter d = 43.96 Å. This pore size value for activated C_{60} corresponds to a mesoporous material of a catalyst support that provides an accessible surface area to the catalyst and to promote the diffusion of chemical species.

Second, the pore size of the $C_{60}Pt_4$ and C_{60} activated systems has been calculated through manually radial distribution function (RDF). The area under RDF curves shown in Figures A2 and A3 is calculated using software GeoGebra. First, Figure A2 corresponds to the following polynomial function for $C_{60}Pt_4$ system:

$$f(x) = x^{20} + x^{19} - x^{18} + x^{17} - x^{16} + x^{15} - x^{14} + x^{13} - x^{12} + x^{11} - x^{10} + x^9 - 0.02x^8 + 0.29x^7 - 2.67x^6 + 18.08x^5 - 86.19x^4 + 272.38x^3 - 523.31x^2 + 530.91x - 179.72$$

Data of this polynomial function has correlation coefficient of 0.996270 and error

of 0.06700. Second, Figure A3 corresponds to the following polynomial function for the activated C_{60} is:

$$f(x) = x^{16} - x^{15} + x^{14} - x^{13} + x^{12} - x^{11} + x^{10} - x^9 + x^8 - x^7 + 0.04 x^6 - 0.43x^5 + 3.46x^4 - 18.31x^3 + 58.31x^2 - 96.63x + 90.75$$

Data provided by this polynomial function has correlation coefficient of 0.996259 and error of 0.06791.

Notice that the surface area of C_{60} fullerene is 1105.33Å^2 as mentioned previously. The area under the curve of the $C_{60}Pt_4$ system which has the polynomial function of 20 grade is A=1200.68 Å^2. Then, pore size diameter is d = 39.09 Å or radius r = 19.54 Å. For the case of C_{60} activated, the area under the curve having the polynomial function of degree 16 is A = 1337.5 Å^2. Then, pore size diameter is d = 41.26 Å or radius r = 20.63 Å. this is only one point of the pore size distribution (psd), which according to measurements of micropore size distribution (mspd) for activated carbon through $ZnCl_2$ [110] the most populated results remain at 9 Å among the distribution range of 6 Å to 18 Å. In this case, the pore size values correspond to mesoporous size of C_{60} catalytic support, to provide an accessible surface area to the catalyst and to stimulate the diffusion of chemical species.

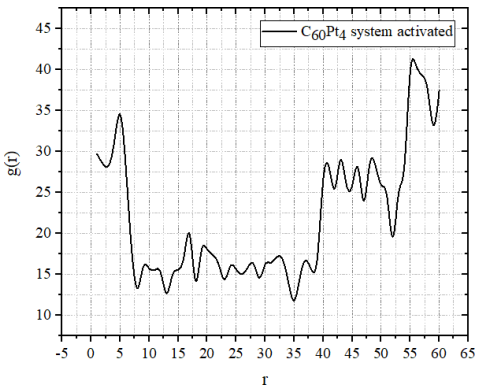

Figure A2. Radial Distribution Function of $C_{60}Pt_4$ system activated

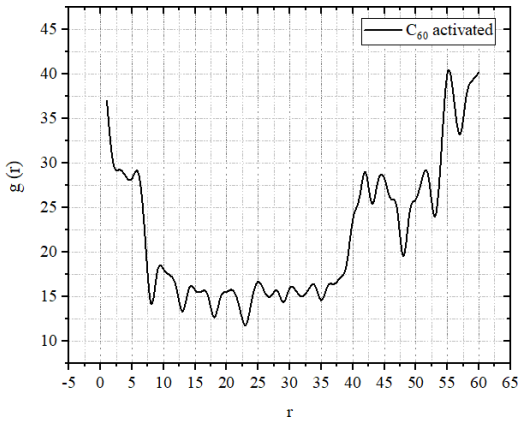

Figure A3. Radial Distribution Function of C_{60} activated.

ACKNOWLEDGEMENTS

The authors would like to express their sincere thanks to the "LA SECTEI" (Secretary of Education, Science, Technology and Innovation), Ciudad de México for the post-doctoral scholarship and for the facilities for the development of the research, because without his support it would not have been possible to carry out this work.

REFERENCES

1 A. Z. Weber and J. Newman, *Modeling Gas-Phase Transport in Polymer-Electrolyte Fuel Cells*, 2019, vol. 1.

2 M. Winter and R. J. Brodd, *Chem. Rev.*, 2004, **104**, 4245–4269.

3 M. K. Debe, *Nature*, 2012, **486**, 43–51.

4 L. Du, Y. Shao, J. Sun, G. Yin, J. Liu and Y. Wang, *Nano Energy*, 2016, **29**, 314– 322.

5 E. L. Jablonski, J. L. G. Fierro, M. C. Román-Martı´nez, S. R. de Miguel, D. Cazorla- Amorós and O. A. Scelza, *J. Catal.*, 2002, **184**, 514–525.

6 F. Coloma, A. Sepúlveda-Escribano, J. L. G. Fierro and F. Rodríguez-Reinoso, *Langmuir*, 1994, **10**, 750–755.

7 H. A. Gasteiger, S. S. Kocha, B. Sompalli and F. T. Wagner, *Appl. Catal. B Environ.*, 2005, **56**, 9–35.

8 W. Gu, D. R. Baker, Y. Liu and H. A. Gasteiger, *Handb. Fuel Cells*, 2010, 1–27.

9 Z. F. Li, L. Xin, F. Yang, Y. Liu, Y. Liu, H. Zhang, L. Stanciu and J. Xie, *Nano Energy*, 2015, **16**, 281–292.

10 M. J. Eslamibidgoli, J. Huang, T. Kadyk, A. Malek and M. Eikerling, *Nano Energy*, 2016, **29**, 334–361.

11 N. Cheng, Y. Shao, J. Liu and X. Sun, *Nano Energy*, 2016, **29**, 220–242.

12 I. Katsounaros, S. Cherevko, A. R. Zeradjanin and K. J. J. Mayrhofer, *Angew. Chemie - Int. Ed.*, 2014, **53**, 102–121.

13 F. Xiao, G. L. Xu, C. J. Sun, I. Hwang, M. Xu, H. wen Wu, Z. Wei, X. Pan, K. Amine and M. Shao, *Nano Energy*, 2020, **77**, 105192.

14 N. V. Long, Y. Yang, C. Minh Thi, N. Van Minh, Y. Cao and M. Nogami, *Nano Energy*, 2013, **2**, 636–676.

15 Z. Zeng and J. Greeley, *Nano Energy*, 2016, **29**, 369–377.

16 P. Strasser and S. Kühl, *Nano Energy*, 2016, **29**, 166–177.

17 S. Cherevko, N. Kulyk and K. J. J. Mayrhofer, *Nano Energy*, 2016, **29**, 275–298.

18 Y. Shao, G. Yin, Y. Gao and P. Shi, *J. Electrochem. Soc.*, 2006, **153**, A1093.

19 Y. Shao, G. Yin and Y. Gao, *J. Power Sources*, 2007, **171**, 558–566.

20 M. C. Smith, J. A. Gilbert, J. R. Mawdsley, S. Seifert and D. J. Myers, *J. Am. Chem. Soc.*, 2008, **130**, 8112–8113.

21 P. Trogadas, J. Parrondo, F. Mijangos and V. Ramani, *J. Mater. Chem.*, 2011, **21**, 19381–19388.

22 M. P. Rodgers, L. J. Bonville, R. Mukundan, R. L. Borup, R. Ahluwalia, P. Beattie, R. P. Brooker, N. Mohajeri, H. R. Kunz, D. K. Slattery and J. M. Fenton, *ECS Trans.*, 2013, **58**, 129–148.

23 A. F. Pedersen, E. T. Ulrikkeholm, M. Escudero-Escribano, T. P. Johansson, P. Malacrida, C. M. Pedersen, M. H. Hansen, K. D. Jensen, J. Rossmeisl, D. Friebel, A. Nilsson, I. Chorkendorff and I. E. L. Stephens, *Nano Energy*, 2016, **29**, 249–260.

24 K. J. J. Mayrhofer, S. J. Ashton, J. C. Meier, G. K. H. Wiberg, M. Hanzlik and M. Arenz, *J. Power Sources*, 2008, **185**, 734–739.

25 K. Hartl, M. Hanzlik and M. Arenz, *Energy Environ. Sci.*, 2011, **4**, 234–238.

26 J. C. Meier, C. Galeano, I. Katsounaros, A. A. Topalov, A. Kostka, F. Schüth and K. J. J. Mayrhofer, *ACS Catal.*, 2012, **2**, 832–843.

27 J. C. Meier, I. Katsounaros, C. Galeano, H. J. Bongard, A. A. Topalov, A. Kostka, A. Karschin, F. Schüth and K. J. J. Mayrhofer, *Energy Environ. Sci.*, 2012, **5**, 9319– 9330.

28 K. Yu, D. J. Groom, X. Wang, Z. Yang, M. Gummalla, S. C. Ball, D. Myers and P. J. Ferreira, *Microsc. Microanal.*, 2014, **20**, 482–483.

29 D. J. Suh, T.-J. Park, J.-H. Kim and K.-L. Kim, *Chem. Mater.*, 2002, **9**, 1903–1905.

30 E. Antolini, *Appl. Catal. B Environ.*, 2009, **88**, 1–24.

31 F. Xu, M. X. Wang, L. Sun, Q. Liu, H. F. Sun, E. A. Stach and J. Xie, *Electrochim. Acta*, 2013, **94**, 172–181.

32 M. X. Wang, Q. Liu, H. F. Sun, N. Ogbeifun, F. Xu, E. A. Stach and J. Xie, *Mater. Chem. Phys.*, 2010, **123**, 761–766.

33 M. X. Wang, F. Xu, H. F. Sun, Q. Liu, K. Artyushkova, E. A. Stach and J. Xie, *Electrochim. Acta*, 2011, **56**, 2566–2573.

34 W. Yang, X. Wang, F. Yang, C. Yang and X. Yang, *Adv. Mater.*, 2008, **20**, 2579– 2587.

35 S. W. Lee, B. S. Kim, S. Chen, Y. Shao-Horn and P. T. Hammond, *J. Am. Chem. Soc.*, 2009, **131**, 671–679.

36 L. Hu, D. S. Hecht and G. Grüner, *Chem. Rev.*, 2010, **110**, 5790–5844.

37 B. Fang, J. H. Kim, C. Lee and J. S. Yu, *J. Phys. Chem. C*, 2008, **112**, 639–645.

38 C. Baldizzone, S. Mezzavilla, H. W. P. Carvalho, J. C. Meier, A. K. Schuppert, M. Heggen, C. Galeano, J. D. Grunwaldt, F. Schüth and K. J. J. Mayrhofer, *Angew. Chemie - Int. Ed.*, 2014, **53**, 14250–14254.

39 F. Hasché, T. P. Fellinger, M. Oezaslan, J. P. Paraknowitsch, M. Antonietti and P. Strasser, *ChemCatChem*, 2012, **4**, 479–483.

40 Y. Li, Y. Li, E. Zhu, T. McLouth, C. Y. Chiu, X. Huang and Y. Huang, *J. Am. Chem. Soc.*, 2012, **134**, 12326–12329.

41 S. Park, Y. Shao, H. Wan, P. C. Rieke, V. V. Viswanathan, S. A. Towne, L. V. Saraf, J. Liu, Y. Lin and Y. Wang, *Electrochem. commun.*, 2011, **13**, 258–261.

42 R. Chen, J. Yan, Y. Liu and J. Li, *J. Phys. Chem. C*, 2015, **119**, 8032–8037.

43 S. H. Joo, S. J. Choi, I. Oh, J. Kwak, Z. Liu, O. Terasaki and R. Ryoo, *Nature*, 2001, **412**, 169–172.

44 N. Mansor, A. B. Jorge, F. Corà, C. Gibbs, R. Jervis, P. F. McMillan, X. Wang and D. J. L. Brett, *J. Phys. Chem. C*, 2014, **118**, 6831–6838.

45 P. V. Shanahan, L. Xu, C. Liang, M. Waje, S. Dai and Y. S. Yan, *J. Power Sources*, 2008, **185**, 423–427.

46 T. Kim, T. Xie, W. Jung, F. Gadala-Maria, P. Ganesan and B. N. Popov, *J. Power Sources*, 2015, **273**, 761–774.

47 T. Xie, W. Jung, T. Kim, P. Ganesan and B. N. Popov, *J. Electrochem. Soc.*, 2014, **161**, F1489–F1501.

48 R. C. Bansal and M. Goyal, *Activated Adsorption Carbon*, 2005.

49 M. Sevilla and R. Mokaya, *Energy Environ. Sci.*, 2014, **7**, 1250–1280.

50 J. H. Pacheco-Sánchez, I. P. Zaragoza-Rivera and A. Bravo-Ortega, *Rev. Mex. Fis.*, 2017, **63**, 97–110.

51 C. N. Satterfield, *Compr. Chem. Kinet.*, 2004, **Volume 40**, 273–308.

52 G. C. Torres, O. A. Scelza, A. A. Castro, S. R. de Miguel, M. D. Blanco, G. T. Baronetti, E. L. Jablonski, M. A. Pen˜a Jiménez and J. L. G. Fierro, *Appl. Catal. A Gen.*, 2003, **161**, 213–226.

53 R. E. Franklin and P. R. S. L. A, *Proc. R. Soc. London. Ser. A. Math. Phys. Sci.*, 1951, **209**, 196–218.

54 A. E. M. Cristian J. Guerra, Jesus M. Lopez, Said F. Figueredo, *Quim. Nova*, 2015, **X**, 1–6.

55 P. J. F. Harris, Z. Liu and K. Suenaga, *Condens. Matter*, 2008, 1–12.

56 56 P. J. . F. Harris, *Int. Mater. Rev.*, 1997, **42**, 206–218.

57 Z. Chen, H. Jiao, M. Bühl, A. Hirsch and W. Thiel, *Theor. Chem. Acc.*, 2001, **106**, 352–363.

58 E. R. Haddon, L. Schneemeyer, J. Waszczak, S. Glarum, R. Tycko, G. Dabbagh and Al., *Nature*, 1991, **354**, 56–58.

59 R. Zanasi, P. Lazzeretti and P. W. Fowler, *Chem. Phys. Lett.*, 1997, **278**, 251–255.

60 A. (Arman) Taherpour, N. Zolfaghar, M. Jamshidi, J. Jalilian, O. Rezaei and Z. Shahri, *J. Mol. Struct.*, 2019, **1184**, 546–556.

61 Y. H. Cheng, J. H. Liao, Y. J. Zhao, J. Ni and X. B. Yang, *Carbon N. Y.*, 2019, **154**, 140–149.

62 Y. Wang, M. Jiao, W. Song and Z. Wu, *Carbon N. Y.*, 2017, **114**, 393–401.

63 X. Chen, J. Chang and Q. Ke, *Carbon N. Y.*, 2018, **126**, 53–57.

64 D. Sankar De, J. A. Flores-Livas, S. Saha, L. Genovese and S. Goedecker, *Carbon N. Y.*, 2018, **129**, 847–853.

65 S. Furmaniak, A. P. Terzyk, P. A. Gauden, P. Kowalczyk and P. J. F. Harris, *J. Phys. Condens. Matter*, , DOI:10.1088/0953-8984/23/39/395005.

66 P. J. F. Harris, *J. Mater. Sci.*, 2013, **48**, 565–577.

67 B. Delley, *J. Chem. Phys.*, 2000, **113**, 7756–7764.

68 B. Delley, *J. Chem. Phys.*, 1990, **92**, 508–517.

69 J. P. Perdew, K. Burke and M. Ernzerhof, *Phys. Rev. Lett.*, 1996, **77**, 3865–3868.

70 F. Hassani and H. Tavakol, *Sensors Actuators, B Chem.*, 2014, **196**, 624–630.

71 D. S. Sabirov and R. G. Bulgakov, *Comput. Theor. Chem.*, 2011, **963**, 185–190.

72 A. Dawid, K. Górny and Z. Gburski, *Spectrochim. Acta - Part A Mol. Biomol. Spectrosc.*, 2015, **136**, 1993–1997.

73 S. Peng and X. J. Li, *Spectrochim. Acta - Part A Mol. Biomol. Spectrosc.*, 2009, **73**, 67–71.

74 R. Vargas, J. Garza and A. Cedillo, *J. Phys. Chem. A*, 2005, **109**, 8880–8892.

75 A. Burian, A. Ratuszna, J. C. Dore and S. W. Howells, *Carbon N. Y.*, 1998, **36**, 1613–1621.

76 C. C. M. Rindt and S. V. Gaastra-Nedea, *Modeling thermochemical reactions in thermal energy storage systems*, Woodhead Publishing Limited, 2015.

77 L. A. Desales Guzmán, J. H. Pacheco Sánchez, G. García Rosales and F. J. Isidro Ortega, *Rev. Mex. Fis.*, 2018, **64**, 634–641.

78 R. G. Parr, *J. Chem. Inf. Model.*, 2013, **53**, 1689–1699.

79 R. G. Parr, R. A. Donnelly, M. Levy and W. E. Palke, *J. Chem. Phys.*, 2003, **68**, 3801–3807.

80 R. G. Parr and R. G. Pearson, *J. Am. Chem. Soc.*, 1983, **105**, 7512–7516.

81 L. R. Domingo, M. J. Aurell, P. Pérez and R. Contreras, *Tetrahedron*, 2002, **58**, 4417–4423.

82 P. Geerlings, F. De Proft and W. Langenaeker, *Chem. Rev.*, 2003, **103**, 1793–1874.

83 A. T. Maynard, M. Huang, W. G. Rice and D. G. Covell, *Proc. Natl. Acad. Sci.*, 2002, **95**, 11578–11583.

84 P. W. Ayers and R. G. Parr, *J. Am. Chem. Soc.*, 2000, **122**, 2010–2018.

85 J. I. Martínez-Araya, G. Salgado-Morán and D. Glossman-Mitnik, *J. Phys. Chem. B*, 2013, **117**, 6339–6351.

86 J. L. Moncada and G. S. Morán, *Quim. Nova*, 2008, **31**, 1255–1258.

87 R. G. Parr, L. V. Szentpály and S. Liu, *J. Am. Chem. Soc.*, 1999, **121**, 1922–1924.

88 D. Glossman-Mitnik, *Procedia Comput. Sci.*, 2013, **18**, 816–825.

89 M. H. Stockett, M. Wolf, M. Gatchell, H. T. Schmidt, H. Zettergren and H. Cederquist, *Carbon N. Y.*, 2018, **139**, 906–912.

90 B. Modak, K. Srinivasu and S. K. Ghosh, *Int. J. Hydrogen Energy*, 2017, **42**, 2278– 2287.

91 M. S. Dresselhaus, G. Dresselhaus and P. C. Eklund, *Sci. Fullerenes Carbon Nanotub.*, 1996, 60–79.

92 H. O. Pierson, *Handb. Carbon, Graph. Diamonds Fullerenes*, 2014, 356–373.

93 A. Nie, J. Wu, C. Zhou, S. Yao, C. Luo, R. C. Forrey and H. Cheng, *Quantum Chem.*, 2007, **107**, 219–224.

94 V. Kumar and Y. Kawazoe, *Phys. Rev. B - Condens. Matter Mater. Phys.*, 2008, **77**, 1–10.

95 Q. Qi, H. Liu, W. Feng, H. Tian, H. Xu and X. Huang, *Comput. Mater. Sci.*, 2015, **96**, 268–276.

96 A. L. Ankudinov, J. J. Rehr, J. J. Low and S. R. Bare, *J. Chem. Phys.*, 2002, **116**, 1911–1919.

97 Y. Liu, M. Lin and Y. Zhao, *J. Phys. Chem. A*, 2017, **121**, 1145–1152.

98 P. BIRKETT, A. AVENT, A. DARWISH, H. KROTO, R. TAYLOR and D. WALTON, *J. Chem. Soc. Chem. Commun.*, 1993, 1230–1232.

99 P. Anto Christy, A. John Peter and C. W. Lee, *Phys. B Condens. Matter*, 2019, **555**, 9–17.

100 L. F. Chaozheng He, Ran Wang, Houyong Yang, Shuo Li, *J. Pre-proofs*, 1990, **394**, 679–698.

101 J. H. Pacheco-Sánchez, *Am. J. Biomed. Sci. Res.*, 2019, **2**, 98–102.

102 X. Chen, J. Chang and Q. Ke, *Carbon N. Y.*, 2018, **126**, 53–57.

103 103 E. Estrada, *J. Phys. Chem. A*, 2002, **106**, 9085–9091.

104 L. A. Desales-Guzmán, J. H. Pacheco-Sánchez, F. J. Isidro-Ortega and K. De la Mora-Zarco, *Int. J. Hydrogen Energy*, 2020, **45**, 6780–6792.

105 J. M. Kim, Y. J. Lee, S. hoon Kim, K. H. Chae, K. R. Yoon, K. A. Lee, A. Byeon, Y. S. Kang, H. Y. Park, M. K. Cho, H. C. Ham and J. Y. Kim, *Nano Energy*, 2019, **65**, 104008.

106 X. Fu, F. M. Hassan, P. Zamani, G. Jiang, D. C. Higgins, J. Y. Choi, X. Wang, P. Xu, Y. Liu and Z. Chen, *Nano Energy*, 2017, **42**, 249–256.

107 T. Yumura, T. Awano, H. Kobayashi and T. Yamabe, *Molecules*, 2012, **17**, 7941– 7960.

108 J. A. Dean, *Properties of atoms, radicals, and bonds.*, 1999.

109 K.P Huber and G. Herzberg, *Molecular Spectra and Molecular Structure*, 1979.

110 D. Lozano-Castelló, D. Cazorla-Amorós and A. Linares-Solano, *Energy and Fuels*, 2002, **16**, 1321–1328.